

Antiferromagnetism and crystalline electric field excitations in tetragonal NaCeO₂

Mitchell M. Bordelon ¹, Joshua D. Bocarsly,² Lorenzo Posthuma,¹ Arnab Banerjee ³,
Qiang Zhang,³ and Stephen D. Wilson ^{1,*}

¹Materials Department, University of California, Santa Barbara, California 93106, USA

²Materials Research Laboratory, University of California, Santa Barbara, California 93106, USA

³Neutron Scattering Division, Oak Ridge National Laboratory, Oak Ridge, Tennessee 37831, USA



(Received 26 October 2020; accepted 4 January 2021; published 19 January 2021)

We investigate the crystal structure, magnetic properties, and crystalline electric field of tetragonal, $I4_1/amd$, NaCeO₂. In this compound, Ce³⁺ ions form a tetragonally elongated diamond lattice coupled by antiferromagnetic interactions ($\Theta_{CW} = -7.69$ K) that magnetically order below $T_N = 3.18$ K. The Ce³⁺ $J = 5/2$ crystalline electric field-split multiplet is studied via inelastic neutron scattering to parametrize a $J_{\text{eff}} = 1/2$ ground state doublet composed of states possessing mixed $|m_z\rangle$ character. Neutron powder diffraction data reveal the onset of A -type antiferromagnetism with $\mu = 0.57(2)\mu_B$ moments aligned along the c axis. The magnetic structure is consistent with the expectations of a frustrated Heisenberg J_1 - J_2 model on the elongated diamond lattice with effective exchange values $J_1 > 4J_2$ and $J_1 > 0$.

DOI: [10.1103/PhysRevB.103.024430](https://doi.org/10.1103/PhysRevB.103.024430)

I. INTRODUCTION

Due to their highly localized moments and their ability to incorporate within a wide variety of frustrated lattice geometries, studying magnetic interactions in lanthanide-based materials is a rich test bed for numerous model Hamiltonians. Perhaps most prominently, rare-earth pyrochlores with the general formula $L_2M_2O_7$ (L = lanthanide; M = metal or metalloid) display unusual magnetic phases like (quantum) spin ice and (quantum) spin liquids [1–16], order by disorder phenomena [17–20], and hidden multipolar order [21–30]. This results from their three-dimensional network of frustrated trivalent lanthanide moments. More recently, layered trivalent lanthanide triangular lattice compounds also have shown promise to exhibit model quantum disordered states, for example, the materials YbMgGaO₄ [31–42] and NaYbX₂ (X = chalcogenide) [43–51].

The recently reported $I4_1/amd$ tetragonal structure of LiYbO₂ has been suggested as another example of an antiferromagnetically frustrated lanthanide system in a three-dimensionally connected lattice [52]. In this material, the $J_{\text{eff}} = 1/2$ Yb³⁺ moments decorate a bipartite lattice that can be interpreted as an extreme elongation of the magnetic diamond lattice. In fact, the simplest magnetic model for the diamond lattice, the Heisenberg J_1 - J_2 model in Eq (1), was adapted to model the incommensurate spiral magnetic order observed in LiYbO₂, where the propagation wave vector is directly ascertained by the ratio of $J_2/|J_1|$ [52]:

$$H = J_1 \sum_{\langle i,j \rangle} \mathbf{S}_i \cdot \mathbf{S}_j + J_2 \sum_{\langle\langle i,j \rangle\rangle} \mathbf{S}_i \cdot \mathbf{S}_j \quad (1)$$

How the ground state evolves as anisotropies, lattice distances, and exchange pathways are modified in these stretched

diamond lattice $I4_1/amd$ materials within the ALX_2 family (A = alkali; L = lanthanide; X = chalcogen) remains unexplored. The spin-orbit entangled lanthanide moments can host a variety of local anisotropies, which can result in a diversity of behaviors across the L ion materials on the same crystallographic framework. Furthermore, the variation in the L ion and A -site cation sizes should alter the ratio of $J_2/|J_1|$ and sample different sections of the phase space of the frustrated Heisenberg model. For instance, it is known that when J_1 and J_2 compete, spiral order emerges as the ground state [52]; however, in the limit where either interaction dominates, conventional Néel or ferromagnetic order should arise.

In this paper, we study the magnetic behavior and ground state of NaCeO₂ [Fig. 1(a)], which shares the same crystallographic structure as LiYbO₂ in the ALX_2 materials family. We show that the Ce³⁺ moments are described by a well-separated $J_{\text{eff}} = 1/2$ Kramers ground state doublet, and inelastic neutron scattering data determine the level structure for the split $J = 5/2$ ground state multiplet. Low-temperature magnetization, heat capacity, and neutron diffraction measurements reveal that NaCeO₂ magnetically orders below $T_N = 3.18$ K into the A -type antiferromagnetic phase shown in Fig. 1(b). This ground state matches the predictions of a J_1 - J_2 Heisenberg model with a dominant nearest-neighbor $J_1 > 0$ interaction.

II. METHODS

A. Sample preparation

As has been previously reported, NaCeO₂ can be prepared by reducing CeO₂ in the presence of liquid sodium [53–55]. Here, we synthesized polycrystalline samples of NaCeO₂ from a 1.1:1.0 molar ratio of Na (99.95% Alfa Aesar) and CeO₂ (99.99% Alfa Aesar), respectively, in sealed 316 stainless-steel tubes, following a synthesis method similar to that previously reported for NaTiO₂ [56]. Reagents were

*stephendwilson@ucsb.edu

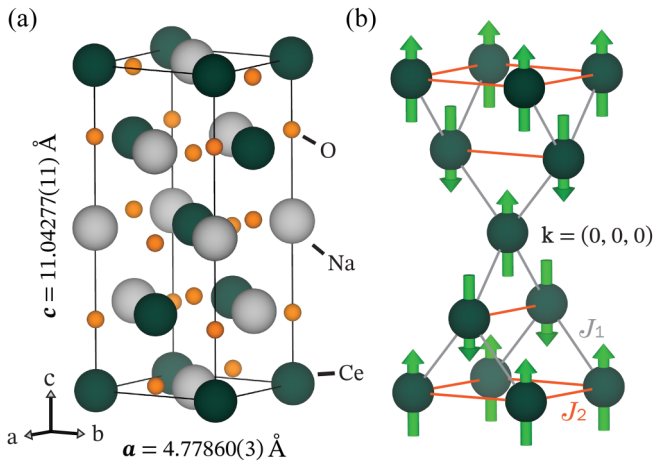


FIG. 1. (a) Schematic of the 1.5 K refined crystal structure from neutron powder diffraction in origin setting 2 of $I4_1/amd$. Trivalent Ce ions reside in D_{2d} distorted CeO_6 octahedra that form a bipartite, tetragonally elongated diamond lattice. (b) The corresponding magnetic structure below $T_N = 3.18$ K contains $0.57(2)\mu_B$ Ce moments oriented parallel to the c axis. Magnetic interactions along J_1 and J_2 are at distances 3.65105 and 4.77860 Å, respectively, where both contain a superexchange pathway with one oxygen atom.

inserted into the steel tubes in an argon-filled glove box with oxygen and water content below 0.5 ppm, and the tube was sealed within the glove box. The capped steel tubes were then placed into a tube furnace and held under vacuum at 1000 °C for three days and were subsequently opened in a glove box. The resulting green NaCeO_2 powder rapidly degrades when in contact with air and moisture, and therefore, it was handled solely in dry, inert environments. Sample composition was verified via x-ray diffraction measurements under Kapton film on a Panalytical Empyrean powder diffractometer with $\text{Cu } K\alpha$ radiation, and data were analyzed using the Rietveld method in the FULLPROF software suite [57].

B. Magnetic susceptibility and heat capacity

Bulk magnetic properties of NaCeO_2 were measured on a Quantum Design magnetic properties measurement system (MPMS3) with a 7-T magnet and a Quantum Design physical properties measurement system (PPMS) with a 14-T magnet and vibrating sample magnetometer. The magnetization of NaCeO_2 was measured from 2 to 300 K under zero-field-cooled (ZFC) and field-cooled (FC) conditions with an applied field of $\mu_0 H = 50$ Oe in the MPMS3. Isothermal magnetization data were collected at 2, 20, 100, and 300 K in the PPMS under fields up to $\mu_0 H = 14$ T. Specific heat measurements were also measured within the PPMS, and heat capacity data were collected between 2 and 300 K on pressed NaCeO_2 in external fields of $\mu_0 H = 0, 3, 5,$ and 9 T.

C. Neutron scattering

Elastic neutron powder diffraction data were obtained from the POWGEN diffractometer at the Spallation Neutron Source at Oak Ridge National Laboratory. A powder sample in a vanadium canister was loaded into a helium-flow cryostat

where data were collected at 1.5 and 10 K in the instrument's Frame 2 (centered at $\lambda = 1.5$ Å) and Frame 3 (centered at $\lambda = 2.665$ Å). Time-of-flight diffraction patterns from both frames were corefined with the TOPAS ACADEMIC software suite [58] for both magnetic and structural phases. Magnetic structural refinements were set up with the aid of ISODISTORT [59,60].

Inelastic neutron scattering data were obtained on the wide Angular-Range Chopper Spectrometer (ARCS) at the Spallation Neutron Source at Oak Ridge National Laboratory. Incident neutrons of energy $E_i = 150$ meV (Fermi 2, Fermi frequency of 600 Hz) were used at $T = 5$ K. Contributions from the aluminum sample can were removed by measuring an empty canister at the same E_i and T . Crystalline electric field analysis utilized a Q -integrated energy cut (E -cut) of the $E_i = 150$ meV ion neutralization spectroscopy (INS) data in the range $|Q| = [5, 6]$ Å⁻¹. Peaks were fit to a pseudo-Voigt function that approximates the beam shape of the instrument.

D. Crystalline electric field analysis

Analysis of the crystalline electric field (CEF) level scheme followed the generic procedure presented in Bordelon *et al.* [45] for NaYbO_2 and Bordelon *et al.* [52] for LiYbO_2 . A synopsis of the procedure is detailed below with changes reflected for NaCeO_2 . NaCeO_2 consists of trivalent Ce^{3+} ions with total angular momentum $J = 5/2$ ($L = 3, S = 1/2; 4f^1$). In the Ce ion's local D_{2d} setting, the $J = 5/2$ manifold can be maximally split into a set of three Kramers doublets. The splitting can be estimated by a point charge (PC) model of ions surrounding a central Ce ion in the crystal field interface of MANTID PLOT [61]. Table I displays three different coordination shell PC models utilizing the refined structural parameters for NaCeO_2 from neutron powder diffraction.

The minimal Hamiltonian with CEF parameters B_n^m and Steven's operators \hat{O}_m^n [62] in D_{2d} symmetry for Ce^{3+} is as follows:

$$H_{\text{CEF}} = B_2^0 \hat{O}_2^0 + B_4^0 \hat{O}_4^0 + B_4^4 \hat{O}_4^4. \quad (2)$$

Diagonalizing the CEF Hamiltonian returns the multiplet's energy eigenvalues, relative probabilities (intensities) of the intramultiplet transitions, wave function basis vectors for each CEF-split doublet, and a powder-averaged g_{avg} factor for the ground state doublet. The PC model approximations were used as starting points for fitting the E -cut of INS data by following a numerical error minimization procedure [45].

III. EXPERIMENTAL RESULTS

A. Crystalline electric field excitations

Inelastic neutron scattering data for NaCeO_2 are displayed in Fig. 2 and were used to determine the $J = 5/2$ CEF scheme of trivalent Ce ions. In Fig. 2(a), two resolution-limited excitations out of the ground state doublet appear and are centered at $E_1 = 117.8$ meV and $E_2 = 124.8$ meV. An energy cut through $I(\mathbf{Q}, \hbar\omega)$ plotted in Fig. 2(b) shows that these excitations are sharp, with lifetimes limited by the instrumental resolution at $E_i = 150$ meV. The CEF strongly separates the ground state Kramers doublet in NaCeO_2 from other states, isolating it as a $J_{\text{eff}} = 1/2$ state at low temperatures. The en-

TABLE I. Point charge (PC) models and the CEF fit for NaCeO₂ obtained by minimizing observed parameters from $E_i = 150$ meV inelastic neutron scattering data and the powder-averaged g_{avg} factor from the magnetic structure. Three PC models represent three coordination shells from a central Ce ion of increasing size, where the first includes only O²⁻ ions, the second has O²⁻ and Na⁺ ions, and the third has O²⁻, Na⁺, and nearest-neighbor Ce³⁺ ions. The fit wave functions are $|\omega_{0,\pm}\rangle = 0.949|\pm 3/2\rangle - 0.316|\mp 5/2\rangle$, $|\omega_{1,\pm}\rangle = |1|\pm 1/2\rangle$, and $|\omega_{3,\pm}\rangle = 0.316|\mp 3/2\rangle + 0.949|\pm 5/2\rangle$.

	E_1	E_2	$\frac{I_2}{I_1}$	g_{avg}	χ^2	B_2^0	B_4^0	B_4^4
PC (2.5 Å)	86.2	122.7	0.763	1.46	8.61	-2.4869	0.2766	1.4544
PC (3.5 Å)	104.6	223.5	0.243	2.07	80.73	-10.2981	0.2645	1.5953
PC (3.7 Å)	53.7	179.3	0.744	1.45	58.78	7.4129	0.2943	1.5249
Fit	117.9	124.8	0.844	1.15	0.0003	0.9254	0.3701	1.3928
Observed	117.8	124.8	0.840	1.14				

ture $J = 5/2$ CEF manifold was fit with extracted parameters from the data in Fig. 2, and the results are shown in Table I and represented schematically in Fig. 2(c). Initial guesses for the fitting procedure were based on PC calculations in Table I. A powder-averaged g factor $g_{\text{avg}} = \sqrt{[1/3(g_{\parallel}^2 + 2g_{\perp}^2)]}$ was utilized as another constraint on the model and was extracted from the ordered moment obtained from the magnetic structure detailed later in this paper ($0.57\mu_B = g_{\text{avg}}J_{\text{eff}}\mu_B$). The final fit of the CEF scheme revealed a ground state wave function with mixed $m_z = 3/2$ and $m_z = 5/2$ character and a moderately anisotropic g tensor ($g_{\parallel} = 1.41$ and $g_{\perp} = 1.00$).

B. Heat capacity, magnetization, and susceptibility results

Magnetic susceptibility and isothermal magnetization data from NaCeO₂ were collected and analyzed between 2 and 300 K, and data are plotted in Fig. 3. Data below 200 K and above T_N were fit to a Curie-Weiss behavior, and constants $\mu_{\text{eff}} = 0.994\mu_B = \sqrt{8C}$, $\Theta_{\text{CW}} = -7.69$ K, and $\chi_0 = 0.0022$ emu mol⁻¹ were extracted from the fit. A peak in the low-

temperature magnetic susceptibility indicative of magnetic ordering was observed at $T_N = 3.4$ K with a corresponding inflection in $d(\chi T)/dT$ at 3.3 K, below which ZFC and FC measurements split. In the ordered state, NaCeO₂ does not saturate up to fields of $\mu_0 H = 14$ T, as shown in Fig. 3(b). Instead, it reaches approximately $0.2\mu_B$, corresponding to only 35% saturation of the expected moment obtained from magnetic structure data detailed in the next section.

Low-temperature specific heat data were also collected between 2 and 300 K in external magnetic fields of $\mu_0 H = 0, 3, 5,$ and 9 T. As shown in Fig. 4, a sharp transition in the zero-field data occurs at $T_N = 3.18$ K, corresponding to the antiferromagnetic transition observed in magnetization measurements. This $C_p(T)$ anomaly softens and lowers in temperature as an increasing external magnetic field partially polarizes the Ce moments. We note here that there is reasonably good agreement between $d(\chi T)/dT$ obtained from susceptibility measurements and the zero-field specific heat [63], where zero-field $C_p(T)$ data reveal $T_N = 3.18$ K close to $d(\chi T)/dT = 3.3$ K determined via $\mu_0 H = 50$ Oe susceptibility.

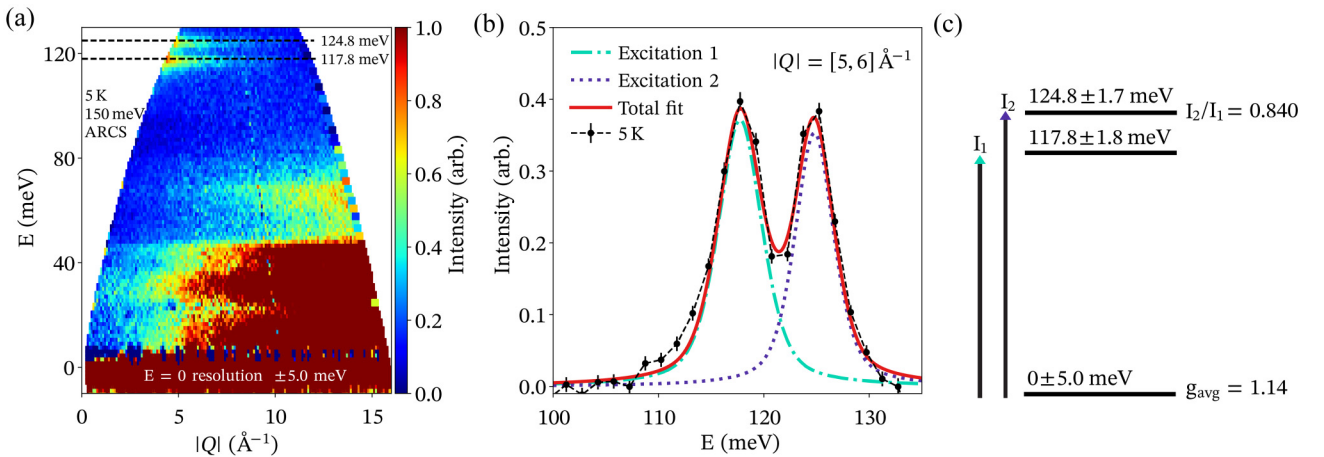


FIG. 2. (a) Inelastic neutron scattering data $I(\mathbf{Q}, \hbar\omega)$ collected at 5 K and $E_i = 150$ meV on the ARCS spectrometer with full width at half maximum energy resolution at the elastic line of 5.0 meV. Two CEF excitations within the $J = 5/2$ Ce³⁺ ground state manifold are indicated by dashed black lines at 117.8 and 124.8 meV. (b) \mathbf{Q} -integrated cut through the data with an empirical linear background subtracted and peak shapes modeled with a pseudo-Voigt function. (c) Schematic of the energy levels of the $J = 5/2$ Ce³⁺ manifold split into three Kramer doublets drawn at 0, 117.8, and 124.8 meV with corresponding full width at half maximum energy resolution of the spectrometer at each energy transfer.

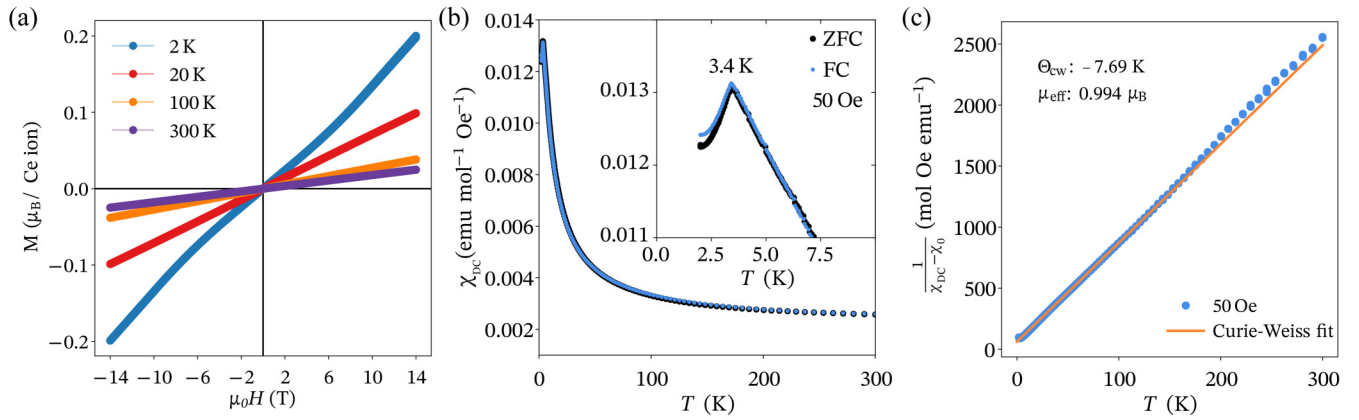


FIG. 3. (a) Isothermal magnetization of NaCeO₂ collected at $T = 2, 20, 100, 300$ K. Below 2 K, NaCeO₂ is magnetically ordered and reaches $0.2\mu_B/\text{Ce}$ at $\mu_0H = 14$ T. (b) Magnetic susceptibility collected under zero-field-cooled (ZFC) and field-cooled (FC) conditions with $\mu_0H = 50$ Oe. Inset: Zoom in of the magnetic susceptibility at low temperature showing a splitting of ZFC and FC below 3.4 K. (c) Inverse susceptibility of NaCeO₂ fit in the range $50 < T < 200$ K to the Curie-Weiss relationship where $\mu_{\text{eff}} = g_{\text{avg}}\sqrt{J(J+1)}$, corresponding to $g_{\text{avg}} = 1.15$ with $J = 1/2$.

C. Crystal structure

Elastic neutron powder diffraction data collected at 10 and 1.5 K are shown in Figs. 5 and 6. Results of Rietveld refinements to the structure of NaCeO₂ in the second origin choice of $I4_1/amd$ are presented in Table II. We detect roughly 2.2(1)% of Ce₂O₃ and 2.1(2)% of Na by weight as impurity phases in the diffraction pattern, likely as a result of degradation of NaCeO₂ from trace water and oxygen exposure during sample transport. The primary NaCeO₂ phase shows fully occupied Na, Ce, and O sites in Table II.

Following the radius ratio rule for ALX_2 ($A = \text{alkali}$; $L = \text{lanthanide}$; $X = \text{chalcogenide}$) materials, NaCeO₂ crystallizes

in the $I4_1/amd$ space group structure [52]. This structure contains D_{2d} CeO₆ distorted, edge-sharing octahedra in a bipartite tetragonally elongated diamond lattice. Nearest-neighbor Ce-Ce distances span J_1 (3.65105 Å), and next-nearest-neighbor Ce-Ce distances are coupled by J_2 (4.77860 Å) in Fig. 1(b). Despite their relatively large difference of roughly 1.1 Å, oxygen-mediated superexchange is promoted along J_2 with a Ce-O-Ce bond angle at 164° relative to J_1 , where the Ce-O-Ce bond angle is 98° . In fact, the Ce-O-Ce distances of J_1 and J_2 are relatively similar at 4.834 and 4.827 Å, respectively. A similar situation has been observed in the related material LiYbO₂, where, in the Heisenberg J_1 - J_2 limit, the bipartite Yb lattice becomes geometrically frustrated when J_1 and J_2 compete and can form a variety of ferromagnetic, antiferromagnetic, and spiral magnetic phases [52].

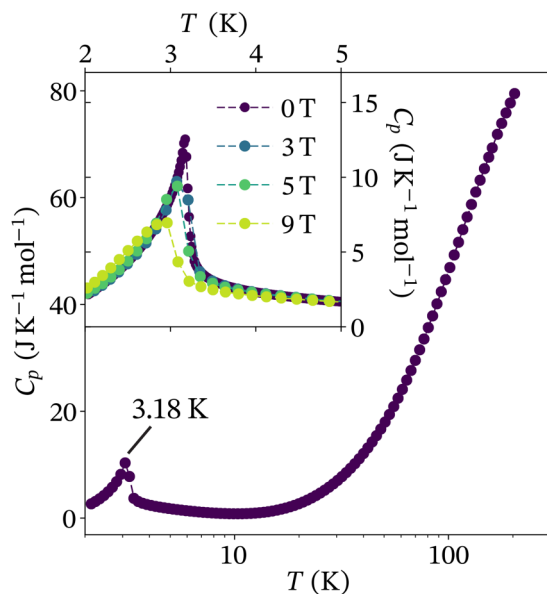


FIG. 4. Specific heat $C_p(T)$ of NaCeO₂ measured under $\mu_0H = 0, 3, 5, 9$ T fields. The onset of antiferromagnetic order occurs at $T_N = 3.18$ K.

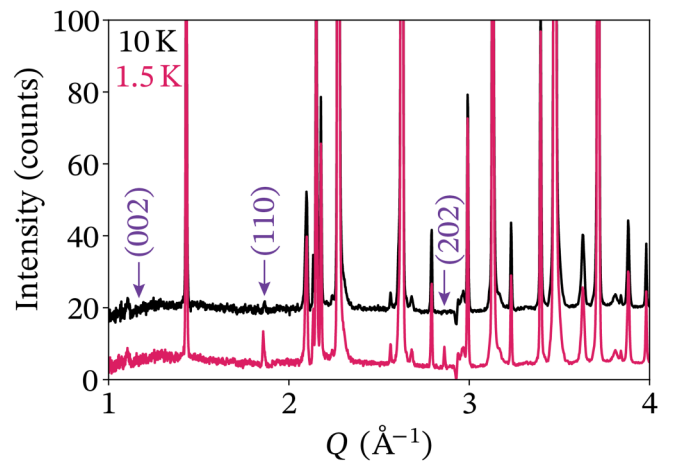


FIG. 5. Neutron diffraction data collected on POWGEN in Frame 3 at 10 K (black) and 1.5 K (pink) distinctly show two magnetic reflections indexed at (1,1,0) and (2,0,2) appearing at 1.5 K. The absence of intensity at the (0,0,2) position at 1.5 K indicates that Ce moments align along the c axis.

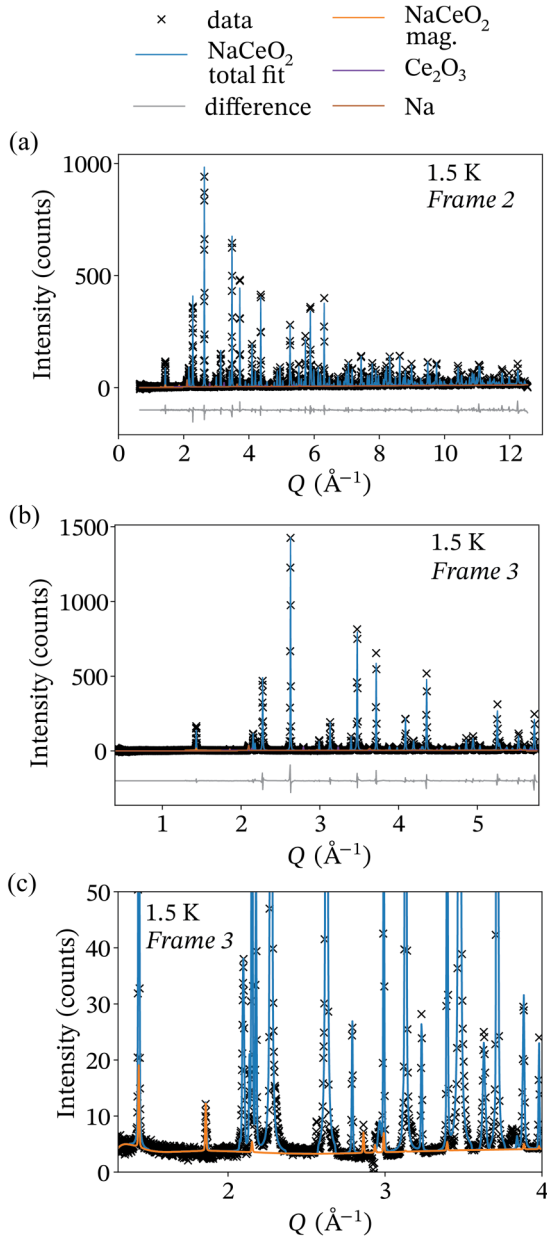


FIG. 6. Elastic neutron diffraction of NaCeO₂ collected on POWGEN at 1.5 K in (a) Frame 2 ($\lambda = 1.5 \text{ \AA}$) and (b) Frame 3 ($\lambda = 2.665 \text{ \AA}$). Data from both frames were corefined to produce the final fit of the data. NaCeO₂ structural parameters are summarized in Table II. Small impurities of 2.2(1)% of Ce₂O₃ and 2.1(2)% of Na by weight were present. (c) A closer look at the total fit and data presented in Frame 3. The refined magnetic structure is an A-type antiferromagnet with an ordered moment of $0.57(2)\mu_B$.

We also note that in the $I4_1/amd$ crystallographic structure, the (1,1,0) reflection is naively forbidden. However, weak intensity at the (1,1,0) position appears in the 10 K data in Fig. 5, suggesting either a weak violation of the $I4_1/amd$ space group in the nuclear structure of NaCeO₂ or that a portion of the NaCeO₂ powder had not fully thermalized at 10 K after warming from 1.5 K. For this analysis, this weak violation was ignored, and both nuclear and magnetic structures were analyzed in the ideal $I4_1/amd$ space group.

TABLE II. Rietveld refinement of structural parameters at 1.5 K from corefined POWGEN Frame 2 and Frame 3 elastic neutron scattering data. NaCeO₂ was modeled in the $I4_1/amd$ space group using origin setting 2. Within error, all ions refine to full occupation, and no site mixing is observed. Data were collected at $T = 1.5 \text{ K}$, and lattice parameters were determined to be $a = b = 4.77860(3) \text{ \AA}$, and $c = 11.04277(11) \text{ \AA}$.

Atom	Wyckoff	x	y	z	$B_{\text{iso}} (\text{\AA}^2)$	Occupancy
Ce	4a	0	0	0	0.057(20)	0.992(5)
Na	4b	0	0	0.5	0.564(20)	1.000(4)
O	8e	0	0	0.21921(9)	0.284(11)	1.000(2)

D. Magnetic structure

Neutron diffraction data collected on NaCeO₂ further show that new magnetic reflections develop below $T_N = 3.18 \text{ K}$, as shown in Fig. 5. Examining the 1.5 K data reveals two distinct magnetic reflections indexed to $\mathbf{Q} = (1,1,0)$ and $\mathbf{Q} = (2,0,2)$. The magnetic reflections at 1.5 K were therefore indexed to a commensurate ordering wave vector $\mathbf{k} = (0, 0, 0)$. No discernible intensity arises at the $\mathbf{Q} = (0,0,2)$ position, indicating the spins lie parallel to the c axis in the ordered phase. The antiferromagnetic structure is generated by the Γ_7 irreducible representation in $I4_1/amd$ and is shown in Fig. 1(b). Moments within the ab plane coalign, and moments along the c axis antialign in an A-type pattern of antiferromagnetic order in the $I4_1'/a'm'd$ magnetic space group. Similar magnetic reflection conditions and structures have been observed in other antiferromagnetic materials sharing the $I4_1/amd$ or related $I4_1/a$ space group (e.g., YbVO₄, KRuO₄ [64,65]). Rietveld refinement of the magnetic structure using this model reveals an ordered Ce³⁺ moment of $0.57(2)\mu_B$. This indicates an average g factor $g_{\text{avg}} = 1.14$, a value consistent with independent susceptibility measurements of $g_{\text{avg}} = 1.15$ in Fig. 3(c).

IV. DISCUSSION

NaCeO₂ provides as an important example of a commensurate magnetically ordered state in the phase diagram of $J_{\text{eff}} = 1/2$ moments decorating the tetragonally elongated diamond lattice of ALX_2 compounds. This commensurate phase differs from a recent report studying the magnetic ground state in LiYbO₂ [52], where it was reported that LiYbO₂ forms an incommensurate spiral magnetic phase in zero field below $T_{\text{AF}} \approx 1 \text{ K}$ with an ordering wave vector $\mathbf{k} = (0.384, \pm 0.384, 0)$.

The magnetic order in LiYbO₂ was previously analyzed by adapting the frustrated diamond lattice Heisenberg J_1 - J_2 model [7–9,17,18] in the extreme limit of tetragonal distortion. Here, the ordering wave vector is uniquely determined by the ratio of $J_2/|J_1|$. The same tetragonal Heisenberg model also predicts a commensurate Néel phase in the limit where $J_1 > 4J_2$ and $J_1 > 0$. This commensurate magnetic state coincides with the structure determined for NaCeO₂ and suggests that the antiferromagnetic J_1 term dominates over J_2 in NaCeO₂. The ratio of these two exchange energies can therefore seemingly be tuned via relatively small lattice

perturbations and by chemically alloying across the tetragonal variants of the ALX_2 series.

The precise mapping of exchange interactions between the two systems, LiYbO_2 and NaCeO_2 , can be modified by anisotropies and other interactions not captured in the minimal Heisenberg J_1 - J_2 Hamiltonian presented in our earlier work [52]. For instance, an XXZ anisotropy can alter the relative phase boundaries since the effect of anisotropy is to renormalize the effective exchange interaction strengths and their ratios. Nevertheless, structural changes between NaCeO_2 and LiYbO_2 , such as relative changes in the L - O - L J_1 bond angles and ratios of L - O bond lengths for J_1 and J_2 pathways, naively should promote a larger J_1/J_2 ratio in NaCeO_2 . This trend and the change in the magnetic ground state are qualitatively consistent with the expectations of the idealized J_1 - J_2 model.

Knowing that spiral and commensurate phases occur in LiYbO_2 and NaCeO_2 , respectively, the entire family of $I4_1/amd$ ALX_2 materials potentially represents a unique opportunity to study the frustrated Heisenberg model in the elongated J_1 - J_2 limit as a function of A and L -ion tunability. Reports have shown that LiLO_2 ($L = \text{Sc, Lu, Er}$) [66] and NaLO_2 ($L = \text{Nd, Sm, Eu, Gd}$) [67] also crystallize in this space group. Some of these materials display sharp antiferromagnetic transitions in specific heat measurements like NaCeO_2 , while others show broad anomalies like LiYbO_2 [52,66] or even ferromagnetic transitions like NaNdO_2 [67]. Future work understanding the impact of varying the lanthanide ion character and single-ion/exchange anisotropies is an appealing next step for further refining the Heisenberg J_1 - J_2 model for these compounds.

V. CONCLUSIONS

The magnetic ground state and crystalline electric field Hamiltonian of Ce ions in the tetragonally elongated diamond lattice of NaCeO_2 were determined. This material crystallizes in the $I4_1/amd$ structure type of the ALX_2 family of compounds, and heat capacity and magnetization measurements show that NaCeO_2 develops long-range magnetic order below $T_N = 3.18$ K. New magnetic reflections appear in neutron powder diffraction data and reveal A -type antiferromagnetic order with an ordered moment of $0.57(2)\mu_B$ per Ce ion. The crystalline electric field scheme of the ground state $J = 5/2$ multiplet was determined, and the ground state wave function was determined to be of mixed $m_z = 3/2$ and $m_z = 5/2$ character. When mapped onto a Heisenberg J_1 - J_2 model, the commensurate antiferromagnetic order observed in this system implies an enhancement in the ratio of effective exchange parameters J_1/J_2 relative to the spiral state formed in LiYbO_2 .

ACKNOWLEDGMENTS

S.D.W. and M.M.B. sincerely thank L. Balents and C. Liu for helpful discussions. This work was supported by the U.S. Department of Energy, Office of Basic Energy Sciences, Division of Materials Sciences and Engineering under Award No. DE-SC0017752 (S.D.W. and M.B.). Research reported here also made use of shared facilities of the UCSB MRSEC (NSF Grant No. DMR-1720256). A portion of this research used resources at the Spallation Neutron Source, a DOE Office of Science User Facility operated by Oak Ridge National Laboratory.

-
- [1] P. A. Lee, *Science* **321**, 1306 (2008).
 - [2] L. Balents, *Nature (London)* **464**, 199 (2010).
 - [3] L. Savary and L. Balents, *Rep. Prog. Phys.* **80**, 016502 (2016).
 - [4] W. Witzczak-Krempa, G. Chen, Y. B. Kim, and L. Balents, *Annu. Rev. Condens. Matter Phys.* **5**, 57 (2014).
 - [5] Y. Zhou, K. Kanoda, and T.-K. Ng, *Rev. Mod. Phys.* **89**, 025003 (2017).
 - [6] C. Broholm, R. Cava, S. Kivelson, D. Nocera, M. Norman, and T. Senthil, *Science* **367**, eaay0668 (2020).
 - [7] S. B. Lee and L. Balents, *Phys. Rev. B* **78**, 144417 (2008).
 - [8] G. Chen, *Phys. Rev. B* **96**, 020412(R) (2017).
 - [9] F. L. Buessen, M. Hering, J. Reuther, and S. Trebst, *Phys. Rev. Lett.* **120**, 057201 (2018).
 - [10] S. Bramwell and M. Harris, *J. Phys.: Condens. Matter* **10**, L215 (1998).
 - [11] M. Harris and M. Zinkin, *Mod. Phys. Lett. B* **10**, 417 (1996).
 - [12] A. P. Ramirez, A. Hayashi, R. J. Cava, R. Siddharthan, and B. Shastri, *Nature (London)* **399**, 333 (1999).
 - [13] S. T. Bramwell and M. J. Gingras, *Science* **294**, 1495 (2001).
 - [14] K. A. Ross, L. Savary, B. D. Gaulin, and L. Balents, *Phys. Rev. X* **1**, 021002 (2011).
 - [15] R. Moessner and J. T. Chalker, *Phys. Rev. Lett.* **80**, 2929 (1998).
 - [16] B. Canals and C. Lacroix, *Phys. Rev. Lett.* **80**, 2933 (1998).
 - [17] D. Bergman, J. Alicea, E. Gull, S. Trebst, and L. Balents, *Nat. Phys.* **3**, 487 (2007).
 - [18] J.-S. Bernier, M. J. Lawler, and Y. B. Kim, *Phys. Rev. Lett.* **101**, 047201 (2008).
 - [19] L. Savary, E. Gull, S. Trebst, J. Alicea, D. Bergman, and L. Balents, *Phys. Rev. B* **84**, 064438 (2011).
 - [20] L. Bellier-Castella, M. J. Gingras, P. C. Holdsworth, and R. Moessner, *Can. J. Phys.* **79**, 1365 (2001).
 - [21] V. K. Anand, A. K. Bera, J. Xu, T. Herrmannsdörfer, C. Ritter, and B. Lake, *Phys. Rev. B* **92**, 184418 (2015).
 - [22] E. Lhotel, S. Petit, S. Guitteny, O. Florea, M. Ciomaga Hatnean, C. Colin, E. Ressouche, M. R. Lees, and G. Balakrishnan, *Phys. Rev. Lett.* **115**, 197202 (2015).
 - [23] H. Takatsu, S. Onoda, S. Kittaka, A. Kasahara, Y. Kono, T. Sakakibara, Y. Kato, B. Fåk, J. Ollivier, J. W. Lynn, T. Taniguchi, M. Wakita, and H. Kadowaki, *Phys. Rev. Lett.* **116**, 217201 (2016).
 - [24] R. Sibille, N. Gauthier, E. Lhotel, V. Porée, V. Pomjakushin, R. A. Ewings, T. G. Perring, J. Ollivier, A. Wildes, C. Ritter, T. C. Hansen, D. A. Keen, G. J. Nilsen, L. Keller, S. Petit, and T. Fennell, *Nat. Phys.* **16**, 546 (2020).
 - [25] K. Tomiyasu, K. Matsuhira, K. Iwasa, M. Watahiki, S. Takagi, M. Wakeshima, Y. Hinatsu, M. Yokoyama, K. Ohoyama, and K. Yamada, *J. Phys. Soc. Jpn.* **81**, 034709 (2012).
 - [26] Y.-D. Li and G. Chen, *Phys. Rev. B* **95**, 041106(R) (2017).
 - [27] O. Benton, *Phys. Rev. B* **94**, 104430 (2016).

- [28] S. Petit, E. Lhotel, B. Canals, M. C. Hatnean, J. Ollivier, H. Mutka, E. Ressouche, A. Wildes, M. Lees, and G. Balakrishnan, *Nat. Phys.* **12**, 746 (2016).
- [29] C. Mauws, A. M. Hallas, G. Sala, A. A. Aczel, P. M. Sarte, J. Gaudet, D. Ziat, J. A. Quilliam, J. A. Lussier, M. Bieringer, H. D. Zhou, A. Wildes, M. B. Stone, D. Abernathy, G. M. Luke, B. D. Gaulin, and C. R. Wiebe, *Phys. Rev. B* **98**, 100401(R) (2018).
- [30] J. Gaudet, E. M. Smith, J. Dudemaine, J. Beare, C. R. C. Buhariwalla, N. P. Butch, M. B. Stone, A. I. Kolesnikov, G. Xu, D. R. Yahne, K. A. Ross, C. A. Marjerrison, J. D. Garrett, G. M. Luke, A. D. Bianchi, and B. D. Gaulin, *Phys. Rev. Lett.* **122**, 187201 (2019).
- [31] X. Zhang, F. Mahmood, M. Daum, Z. Dun, J. A. M. Paddison, N. J. Laurita, T. Hong, H. Zhou, N. P. Armitage, and M. Mourigal, *Phys. Rev. X* **8**, 031001 (2018).
- [32] Z. Zhu, P. A. Maksimov, S. R. White, and A. L. Chernyshev, *Phys. Rev. Lett.* **119**, 157201 (2017).
- [33] Y.-D. Li, Y. Shen, Y. Li, J. Zhao, and G. Chen, *Phys. Rev. B* **97**, 125105 (2018).
- [34] Y.-D. Li, X. Wang, and G. Chen, *Phys. Rev. B* **94**, 035107 (2016).
- [35] Y. Li, D. Adroja, P. K. Biswas, P. J. Baker, Q. Zhang, J. Liu, A. A. Tsirlin, P. Gegenwart, and Q. Zhang, *Phys. Rev. Lett.* **117**, 097201 (2016).
- [36] Y. Li, G. Chen, W. Tong, L. Pi, J. Liu, Z. Yang, X. Wang, and Q. Zhang, *Phys. Rev. Lett.* **115**, 167203 (2015).
- [37] Y. Li, H. Liao, Z. Zhang, S. Li, F. Jin, L. Ling, L. Zhang, Y. Zou, L. Pi, Z. Yang, J. Wang, Z. Wu, and Q. Zhang, *Sci. Rep.* **5**, 1 (2015).
- [38] Y. Li, D. Adroja, R. I. Bewley, D. Voneshen, A. A. Tsirlin, P. Gegenwart, and Q. Zhang, *Phys. Rev. Lett.* **118**, 107202 (2017).
- [39] P. A. Maksimov, Z. Zhu, S. R. White, and A. L. Chernyshev, *Phys. Rev. X* **9**, 021017 (2019).
- [40] J. A. Paddison, M. Daum, Z. Dun, G. Ehlers, Y. Liu, M. B. Stone, H. Zhou, and M. Mourigal, *Nat. Phys.* **13**, 117 (2017).
- [41] Y. Shen, Y.-D. Li, H. Wo, Y. Li, S. Shen, B. Pan, Q. Wang, H. C. Walker, P. Steffens, M. Boehm, Y. Hao, D. L. Quintero-Castro, L. W. Harriger, M. D. Frontzek, L. Hao, S. Meng, Q. Zhang, G. Chen, and J. Zhao, *Nature (London)* **540**, 559 (2016).
- [42] Y. Xu, J. Zhang, Y. S. Li, Y. J. Yu, X. C. Hong, Q. M. Zhang, and S. Y. Li, *Phys. Rev. Lett.* **117**, 267202 (2016).
- [43] M. Baenitz, P. Schlender, J. Sichelschmidt, Y. A. Onykienko, Z. Zangeneh, K. M. Ranjith, R. Sarkar, L. Hozoi, H. C. Walker, J.-C. Orain, H. Yasuoka, J. van den Brink, H. H. Klauss, D. S. Inosov, and T. Doert, *Phys. Rev. B* **98**, 220409(R) (2018).
- [44] M. M. Bordelon, E. Kenney, C. Liu, T. Hogan, L. Posthuma, M. Kavand, Y. Lyu, M. Sherwin, N. P. Butch, C. Brown, M. J. Graf, L. Balents, and S. D. Wilson, *Nat. Phys.* **15**, 1058 (2019).
- [45] M. M. Bordelon, C. Liu, L. Posthuma, P. M. Sarte, N. P. Butch, D. M. Pajerowski, A. Banerjee, L. Balents, and S. D. Wilson, *Phys. Rev. B* **101**, 224427 (2020).
- [46] L. Ding, P. Manuel, S. Bachus, F. Grubler, P. Gegenwart, J. Singleton, R. D. Johnson, H. C. Walker, D. T. Adroja, A. D. Hillier, and A. A. Tsirlin, *Phys. Rev. B* **100**, 144432 (2019).
- [47] W. Liu, Z. Zhang, J. Ji, Y. Liu, J. Li, X. Wang, H. Lei, G. Chen, and Q. Zhang, *Chin. Phys. Lett.* **35**, 117501 (2018).
- [48] K. M. Ranjith, D. Dmytriieva, S. Khim, J. Sichelschmidt, S. Luther, D. Ehlers, H. Yasuoka, J. Wosnitza, A. A. Tsirlin, H. Kühne, and M. Baenitz, *Phys. Rev. B* **99**, 180401(R) (2019).
- [49] K. M. Ranjith, S. Luther, T. Reimann, B. Schmidt, P. Schlender, J. Sichelschmidt, H. Yasuoka, A. M. Strydom, Y. Skourski, J. Wosnitza, H. Kühne, T. Doert, and M. Baenitz, *Phys. Rev. B* **100**, 224417 (2019).
- [50] R. Sarkar, P. Schlender, V. Grinenko, E. Haeussler, P. J. Baker, T. Doert, and H.-H. Klauss, *Phys. Rev. B* **100**, 241116(R) (2019).
- [51] J. Sichelschmidt, P. Schlender, B. Schmidt, M. Baenitz, and T. Doert, *J. Phys.: Condens. Matter* **31**, 205601 (2019).
- [52] M. M. Bordelon, C. Liu, L. Posthuma, E. Kenney, M. J. Graf, N. P. Butch, A. Banerjee, S. Calder, L. Balents, and S. D. Wilson, *Phys. Rev. B* **103**, 014420 (2021).
- [53] M. Mignaneli, P. Potter, and M. Barker, *J. Nucl. Mater.* **97**, 213 (1981).
- [54] M. G. Barker, S. A. Frankham, and P. G. Gadd, *J. Inorg. Nucl. Chem.* **43**, 2815 (1981).
- [55] M. G. Barker, S. A. Frankham, and P. G. Gadd, *J. Nucl. Mater.* **218**, 256 (1995).
- [56] D. Wu, X. Li, B. Xu, N. Twu, L. Liu, and G. Ceder, *Energy Environ. Sci.* **8**, 195 (2015).
- [57] J. Rodríguez-Carvajal, *Physica B (Amsterdam, Neth.)* **192**, 55 (1993).
- [58] A. A. Coelho, *J. Appl. Crystallogr.* **51**, 210 (2018).
- [59] H. T. Stokes, D. M. Hatch, and B. J. Campbell, (2019).
- [60] H. T. Stokes, D. M. Hatch, B. J. Campbell, and D. E. Tanner, *J. Appl. Crystallogr.* **39**, 607 (2006).
- [61] O. Arnold *et al.*, *Nucl. Instrum. Methods A* **764**, 156 (2014).
- [62] K. Stevens, *Proc. Phys. Soc. London, Sect. A* **65**, 209 (1952).
- [63] M. E. Fisher, *Philos. Mag.* **7**, 1731 (1962).
- [64] P. Radhakrishna, J. Hammann, and P. Pari, *J. Magn. Magn. Mater.* **23**, 254 (1981).
- [65] C. A. Marjerrison, C. Mauws, A. Z. Sharma, C. R. Wiebe, S. Derakhshan, C. Boyer, B. D. Gaulin, and J. E. Greedan, *Inorg. Chem.* **55**, 12897 (2016).
- [66] Y. Hashimoto, M. Wakeshima, K. Matsuhira, Y. Hinatsu, and Y. Ishii, *Chem. Mater.* **14**, 3245 (2002).
- [67] Y. Hashimoto, M. Wakeshima, and Y. Hinatsu, *J. Solid State Chem.* **176**, 266 (2003).